The Influence of Temperature on the Strength of Hybrid Metal-Composite Multi-Bolts Joints

Calin-Dumitru COMAN*

*Corresponding author
INCAS – National Institute for Aerospace Research "Elie Carafoli",
B-dul Iuliu Maniu 220, Bucharest 061126, Romania,
coman.calin@incas.ro

DOI: 10.13111/2066-8201.2020.12.3.4

Received: 31 May 2020/ Accepted: 30 June 2020/ Published: September 2020

Abstract: *This paper presents the temperature influence on the strength of the hybrid metal-composite multi-bolted joints. A detailed 3D finite element model, incorporating all possible nonlinearities as large deformations, in plane nonlinear shear deformations, elastic properties degradation of the composite material and friction-based full contact, is developed to anticipate the temperature changing effects on the progressive damage analysis (PDA) at lamina level and failure modes of metal-composite multi-bolted joints. The PDA material model accounts for lamina nonlinear shear deformation, Hashin-type failure criteria and strain-based continuum degradation rules being developed using the UMAT user subroutine in Nastran commercial software. In order to validate the temperature effects on the failure modes of the joint with protruding and countersunk bolts, experiments were conducted using the SHM (Structural Health Monitoring) technique in the temperature controlled chamber. The results showed that the temperature effects on damage initiation and failure modes have to be taken into account in the design process in order to fructify the high specific strength of the composites. Experimental results were quite accurately predicted by the PDA material model, which proved to be computational efficient and can predict failure propagation and damage mechanism in hybrid metal-composite multi-bolted joints.*

Key Words: *Hybrid bolted joints, progressive damage analysis, finite element analysis, temperature, joint strength.*

1. INTRODUCTION

The aerospace industry became the most common application field for fiber-reinforced polymer matrix composites (PMCs) due to their lightweight properties [1]. These structural components are often assembled in conjunction with metal parts using mechanically fastened joints resulting in hybrid metal-composite joints which generated some challenging problems for mechanical engineers. Poorly designed hybrid joints is not only a source of failure, but could lead to a reduction in durability and reliability of the whole structure. Up to nowadays, the researchers studied the failure modes of composite bolted joints using a method that combines continuum damage mechanics (CDM) [2] with finite element analysis (FEA). In the CDM models, the local damage onset appears at low values of the applied load, and damage accumulation is developed with increasing load according to damage propagation laws, which makes the method quite accurate and able to predict various failure modes. The major disadvantage of the CDM models is the huge amount of test data required for model

calibrations. The progressive damage analysis (PDA) of composite materials, based on the stress–strain failure criterion, [3], showed that orthotropic properties reduction due to damage is essential for the stress field distribution [4 - 7]. Damage initiation based on the local stress–strain field and stiffness degradation to reflect damage growth were primarily investigated within the framework of CDM, while delamination and matrix cracking were studied using interface fracture mechanics approaches as cohesive zone models (CZM) and virtual crack closure techniques (VCT), [6].

A discrete ply model together with cohesive elements placed at the interfaces between solid elements as to represent matrix cracks and delamination allow the natural coupling between the intra-laminar and inter-laminar damage to be naturally taken into account and can be used for a computational study of scaled open-hole tensile tests, [8], or the failure mode called pull-through for test of fasteners in laminates, [9], where the effects of splitting and load redistribution were correctly predicted. PDA models, [10–14], incorporate shear nonlinearity, Hashin-type failure criterion and constant elastic properties degradation laws, which become quite easy to implement and computationally efficient. Because these properties degradation models used constant factors for elastic properties reduction due to damage growth, the models weren't able to predict the bearing final failure. An innovative design for mechanically fastened joints in composite laminates was proposed by Camanho and Lambert, [10], to predict the final failure load and failure modes using average stress models. A comprehensive review on the available degradation models for PDA containing 310 references was organized by Garnich and Akula, [15], around the relationships of the various models together with the used frameworks for finite element implementation. A continuum-based progressive damage model for fiber-reinforced composites was implemented in the finite element code ABAQUS by Koerber and Camanho, [16], considering two failure modes: catastrophic net-section tension-failure and non-catastrophic accumulation of bearing damage. A lot of models containing continuous degradation rules, started to appear in the open literature, [17, 18], as to improve the numeric algorithm convergence and to obtain a smoother load–displacement curve.

Du et al. [19] used detailed three-dimensional (3D) finite element models established in ABAQUS/Explicit with a VUMAT user subroutine and studied the failure behavior of pultruded fiber-reinforced polymer bolted joints. A major disadvantage of these models is that they have focused on only a few types of failure modes and are not concerned with various joint failure modes. The composite progressive damage mechanism is complex and in conjunction with geometric and contact nonlinearities can lead to divergences of the finite element method (FEM) analysis, mostly in implicit numerical algorithms. The composite materials can withstand temperatures up to 300^0C, having good properties as: high pressure resistance, low thermal expansion coefficient, high thermal conductivity, high thermal shock resistance and low depression, [20]. The difficulties arising from composite materials used on structural failure problems are that these materials have anisotropic mechanical properties, brittle behavior and low interlaminar strength, [21]. Another issue is the damage variation with the temperature as it is described in the literature, [22 - 25]. Various structures can be exposed to rush environment conditions which can imply the joints strength loss because of environmental ageing and temperature variations, [26 - 30].

In this paper, a PDA analysis is developed using an adequate material model for a hybrid metal–composite multi bolts joint which can predict the thermal effects on the joint strength, considering geometric nonlinearity, friction-based contact and material nonlinearity due to the lamina shear deformations. The Hashin failure criterion and strain-based continuous degradation rules were implemented using a user subroutine in the commercial MSC Nastran SOL 400 solver. A series of experiments were conducted as to validate the 3D FE model and

PDA results, involving the influence of temperature on the failure loads and modes of the hybrid metal–composite joints.

2. PROBLEM DESCRIPTION

- Joint geometry description

The geometry of the studied joint model is presented in Figure 1. The dimensions are in accordance with ASTM D 5961 standard, [31] to induce bearing failure. The in plane dimensions of the plates are as follows: 150 mm length 50 mm width. The thicknesses are different, 4 mm for metal adherent and 2 mm for composite plate. A similar geometry was used before in Chishti et al., [32]. The joint under investigation has a close tolerance clearance equal to 48 μm according to f7H10, [33], standard fit tolerances. Protruding and countersunk head stainless steel bolts with nominal diameter of 5 mm and 4 mm were installed with 0.5 Nm torque level applied in dry conditions.

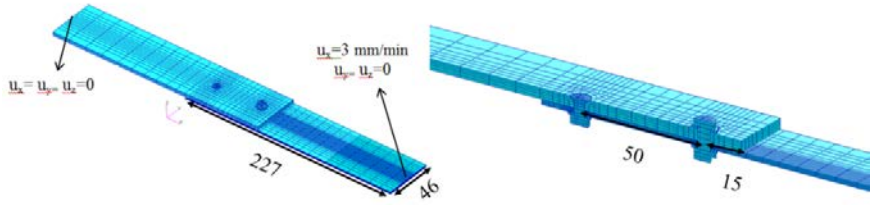

Figure 1. Joint geometry and boundary conditions, all dimensions in mm

The composite plate was manufactured from carbon-epoxy pre-pregs with 32% fiber volume fraction (V_{FIBER}). The stacking sequence is [0/90/0/90/0/90] using 0.33mm thickness unidirectional lamina, with the material properties presented in Table 1. The metal plate was manufactured from aluminum alloy AA 7075T6 and the bolts, nuts and washers were fabricated from stainless steel A2-70 with the material properties presented in Table 2. A group of five specimens were prepared for the thermal effects study on the failure mechanisms in the laminated plate.

- Boundary conditions

Regarding the clamping of the joint in the testing machine, the boundary conditions imposed on the FE model are presented in Figure 1. The displacements *u*, *v* and *w* are defined along *x*, *y* and *z* directions. The boundary conditions represent clamping the nodes on top and bottom surfaces at the end of the aluminum plate and blocking the translations on *y* and *z* directions (*v* and *w*) at the rightmost end of the composite plate only on the surface of the plate over the length of 70 mm each side, which was griped during the test as to agree with the experiment. For simulating the quasi-static loading condition of the testing machine, a prescribed *u* displacement on *x* direction is applied to the nodes from both surfaces of the composite plate at the rightmost end.

Table 1. Composite material properties

Property	Carbon fibers Toray T300 12k [34]	Epoxy matrix Derakane Momentum 411-350 [35]	Lamina Exp.
Longitudinal modulus E_{11} (MPa)	230000	3200	34433
Transversal modulus E_{22} (MPa)	6000	3200	3610
Through-thickness modulus, E_{33} (MPa)	-	3200	3610
In plane shear modulus G_{12} (MPa)	18000	1300	2421

Out of plane shear modulus G_{23} (MPa)	-	1300	2421
Out of plane shear modulus G_{13} (MPa)	-	1300	1561
Poisson coefficient ν_{12}	0.36	0.35	0.36
Poisson coefficient ν_{23}	-	0.35	0.45
Poisson coefficient ν_{13}	-	0.35	0.35
Longitudinal tensile strength $\sigma_{11,\max}^{T}$, (MPa)	3530	86	253
Longitudinal compression strength $\sigma_{11,\max}^{C}$, (MPa)	-	-	230
Transversal compression strength $\sigma_{22,\max}^{C}$, (MPa)	-	-	74
In plane shear strength $\tau_{12}^{\max}$, (MPa)	-	-	25
Out plane shear strength $\tau_{23}^{\max}$, (MPa)	-	-	37
Out plane shear strength $\tau_{13}^{\max}$, (MPa)	-	-	37

Note: (1, 2, 3) system axis is the same as rectangular (x, y, z) system axis from Figure 1.

Table 2. Isotropic material properties for metallic parts, [36]

Property	AA 7075T6 [36]	A2-70 [36]
Elastic modulus, *E* (MPa)	71016	206000
Shear modulus, *G* (MPa)	26890	75842
Poisson coefficient, *v*	0.33	0.36

The unidirectional lamina properties presented in Table 1 were obtained using ASTM standards [37], [38] by performing tests on the unidirectional laminated specimens and are given in Table 1 (Exp.). The shearing deformation was obtained using the Iosipescu test on notched specimens and traction for specimens cut at 45º with respect to the alignment of 0/90º as to obtain fibers at ±45º. The results coming from the Iosipescu specimen testing were used further. Regarding the thermal expansion coefficient of the composite plate, it has been used a micro-analysis method to calculate this coefficient at lamina level using the thermal coefficients of the fibers and matrix. The fibers thermal expansion coefficient is α_{FIBER}= - 0.41 (10^{-6}/ºC), [34] and, α_{MATRIX}= 40 (10^{-6}/ ºC), [35], for the matrix thermal coefficient. Using these values and equation (1), the lamina thermal coefficients on the orthotropic axis can be obtained, [39]:

$$\alpha_{11}=\frac{E_{11\ FIBER}\cdot V_{FIBER}\cdot\boldsymbol{\alpha}_{FIBER}+E_{11\ MATRIX}\cdot(1-V_{FIBER})\cdot\boldsymbol{\alpha}_{MATRIX}}{E_{11}}=2\cdot10^{-6}/C \quad (1)$$

$$\alpha_{22}=\alpha_{33}=44\cdot10^{-6}/C \quad (2)$$

- Experimental setup

After joints installation setup, the specimens were gripped in the 30kN Instron 3367, Figure 2, universal testing machine connected to a temperature controlled chamber. The used chamber is Instron SFL 3119-400 series, temperature controlled (-70/+250ºC), with liquid CO_2 as frozen agent. The bearing tests were conducted in accordance with ASTM D 5961, [31], standard and the specimens were loaded with controlled displacement of 0.3 mm/min until ultimate failure at two temperature values, T= + 50ºC and T= - 50ºC.

- Numerical analysis

A tridimensional finite element model, using linear eight nodes brick elements, was developed in commercial software MSC Patran for the joint model, Figure 3. Each separate part was modeled: metal and composite plates, three washers and two combined bolt-nut parts. The plates were meshed with high radial mesh density around each hole, where high strain gradients exists. In order to avoid rigid body motions, light springs were attached to the components not fully constrained, such as the bolts, washers and laminate plate. For simulating

the bolt preload due to the torque level, a 330 N axial force was applied in the bolt shank using Bolt Preload Module in Patran. This is done by sectioning the bolt shank in the shear plane location which separates the shank in two parts and creates coincident nodes at the interface cutting plane. These coincident nodes are then connected by an over-closure MPC (Multi Points Constrained) and loaded with axial preload.

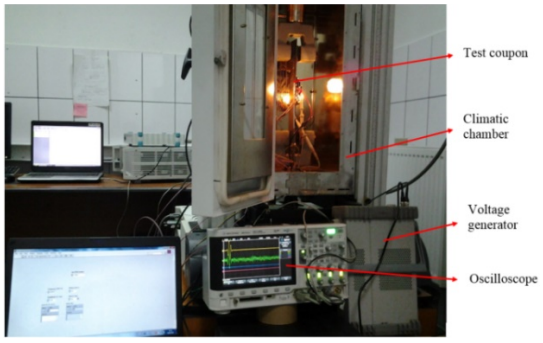

Figure 2. Experimental workbench, [39]

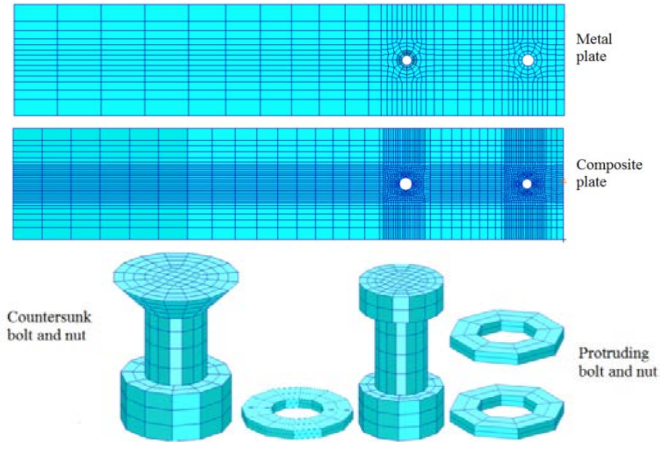

Figure 3. 3D finite element model

The laminated plate is modeled with continuum solid-shell advanced elements available in MSC Nastran 2012. These special solid elements have bending properties like shells. The finite element model has six elements per laminate thickness, with one solid-shell element per each ply. All metallic parts are modeled with continuum solid elements with large strain property assumed. The bolt-hole contact is achieved by a direct method of constraints. The method requires the definition of contact bodies. The contact bodies may be the physical parts, but it has been shown, [40], that it is more efficient to consider sets of elements of these parts, Figure 4, due to runtime reducing.

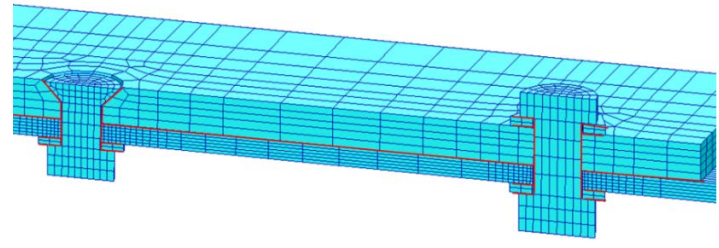

Figure 4. Contact elements in 3D model

3. TEMPERATURE EFFECTS ON THE FAILURE MECHANISM

- Nonlinear shear strains

In order to take into account the nonlinear behavior of the composite plate within the hybrid metal-composite joint, the simulation must account for the two most important nonlinear mechanisms: lamina nonlinear shear deformations and stiffness reduction due to damage accumulation at lamina level. These two nonlinearities are considered by using an external user-defined subroutine named *User_mat*, edited in FORTAN language. *User_mat* calls the modified predefined MSC. Nastran subroutine UMAT, in order to implement the material nonlinearities specified above. Hahn and Tsai, [41], developed the in plane nonlinear shear lamina constitutive model using high order elasticity theory:

$$\gamma_{12} = \frac{\tau_{12}}{G_{12}} + \beta \cdot \tau_{12}^3 \tag{3}$$

where β is a material parameter that can be determined only by experiments, see Figure 5. This constitutive relation can be implemented in *User_mat* subroutine as it is described in [42]:

$$\tau_{12}^{(t+\Delta t)} = \frac{1+2\cdot\beta\cdot(\tau_{12}^t)^3\cdot(\gamma_{12}^t)^{-1}}{1+3\cdot\beta\cdot G_{12}{}^0\cdot(\tau_{12}^{(i)})^2}\cdot G_{12}{}^0\cdot\gamma_{12}^{t+\Delta t} \tag{4}$$

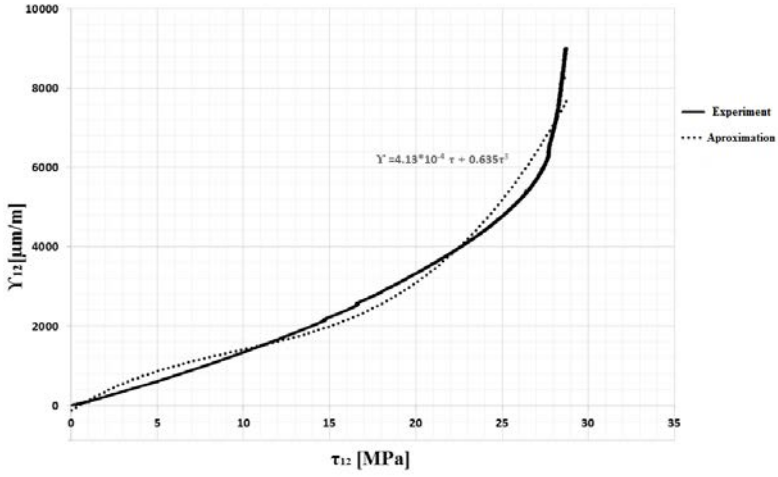

Figure 5. Nonlinear shear stress–strain experimental curve

The orthotropic stress-strain constitutive relationship is given by equations (5) and (6), according to [42]:

$$\begin{bmatrix}\sigma_{11}^{t+\Delta t}\\ \sigma_{22}^{t+\Delta t}\\ \sigma_{33}^{t+\Delta t}\end{bmatrix} = \begin{bmatrix} E_{11}B(1-\nu_{23}\nu_{32}) & E_{22}B(\nu_{12}-\vartheta_{13}\vartheta_{32}) & E_{33}B(\nu_{13}-\nu_{12}\nu_{23})\\ E_{22}B(\nu_{12}-\nu_{13}\nu_{32}) & E_{22}B(1-\nu_{13}\nu_{31}) & E_{22}B(\nu_{32}-\nu_{12}\nu_{31})\\ E_{33}B(\nu_{13}-\nu_{12}\nu_{23}) & E_{22}B(\nu_{32}-\nu_{12}\nu_{31}) & E_{33}B(1-\nu_{12}\nu_{21})\end{bmatrix} \times \begin{bmatrix}\varepsilon_{11}^{t+\Delta t}\\ \varepsilon_{22}^{t+\Delta t}\\ \varepsilon_{33}^{t+\Delta t}\end{bmatrix} \tag{5}$$

$$\begin{bmatrix}\tau_{12}^{t+\Delta t}\\ \tau_{23}^{t+\Delta t}\\ \tau_{31}^{t+\Delta t}\end{bmatrix} = \begin{bmatrix} Rel.(8) & 0 & 0\\ 0 & G_{23} & 0\\ 0 & 0 & G_{31}\end{bmatrix} \times \begin{bmatrix}\gamma_{12}^{t+\Delta t}\\ \gamma_{23}^{t+\Delta t}\\ \gamma_{31}^{t+\Delta t}\end{bmatrix} \tag{6}$$

where:

$$B=\frac{1}{1-\nu_{12}\nu_{21}-\nu_{23}\nu_{32}-\nu_{13}\nu_{31}-2\cdot\nu_{21}\nu_{32}\nu_{13}} \tag{7}$$

$$\tau_{12}^{t+\Delta t}=\begin{cases}\dfrac{1+2\cdot\beta\cdot(\tau_{12}^{t})^{3}\cdot(\gamma_{12}^{t})^{-1}}{1+3\cdot\beta\cdot {G_{12}}^{0}\cdot(\tau_{12}^{t})^{2}}\cdot {G_{12}}^{0}\cdot\gamma_{12}^{(t+\Delta t)}, & FI=0\\ {G_{12}}^{t+\Delta t}\cdot\gamma_{12}^{t+\Delta t}, & FI\geq 1 \text{ and } {G_{12}}^{t+\Delta t}\cdot\gamma_{12}^{t+\Delta t}<\tau_{12}^{init}\\ \tau_{12}^{init}, & FI\geq 1 \text{ and } {G_{12}}^{t+\Delta t}\cdot\gamma_{12}^{t+\Delta t}\geq\tau_{12}^{init}\end{cases} \tag{8}$$

$$FI=max(FI_1,FI_2) \tag{9}$$

In relation (8), ${G_{12}}^{0}$ is the initial in-plane shear modulus which is reduced according to degradation rules specified in relation (13), once the fiber compression-shear failure occurs. The shear stress τ_{12}^{init} is a threshold used to avoid any over-estimation of the shear stress after any failure that can reduce the shear modulus G_{12}.

- Failure criteria and continuous degradation rules

The most dominant micro-failure modes for bearing joints are matrix compression and fiber shear-compression failures, so a great attention is paid to them in this study. For the PDA analysis of the laminated plate around the hole, Hashin [43] failure criteria is used and the failure indexes are calculated using relation (10) for matrix compression and (11) for compression-shear fiber:

$$FI_1=\left[\left(\frac{\sigma_{22,\max}^{C}}{2\cdot\tau_{23}^{\max}}\right)^2-1\right]\cdot\frac{\sigma_2+\sigma_3}{\sigma_{22,\max}^{C}}+\frac{(\sigma_2+\sigma_3)^2}{4\cdot\left(\tau_{23}^{\max}\right)^2}-\frac{\sigma_2\cdot\sigma_3}{\left(\tau_{23}^{\max}\right)^2}+\left(\frac{\tau_{12}}{\tau_{12}^{\max}}\right)^2+\left(\frac{\tau_{13}}{\tau_{13}^{\max}}\right)^2+\left(\frac{\tau_{23}}{\tau_{23}^{\max}}\right)^2+\left(\frac{\sigma_1}{\sigma_{11,\max}^{T}}\right)^2 \tag{10}$$

$$FI_2=\left(\frac{\sigma_1}{\sigma_{11,\max}^{C}}\right)^2+\left(\frac{\tau_{12}}{\tau_{12}^{\max}}\right)^2+\left(\frac{\tau_{13}}{\tau_{13}^{\max}}\right)^2 \tag{11}$$

- Continuous degradation rules for elastic longitudinal moduli

A strain based degradation rule is proposed for reduction of E_{ii} (i=1…3) as described in [43]. The fiber or matrix failure initiate at a user-defined failure strain ε_{ii}^{init} and PDA stiffness reductions are performed using:

$$E_{ii}^{t+\Delta t}=\begin{cases}E_{ii}^{0}\cdot\left(1-d_i\cdot\dfrac{\varepsilon_{ii}^{t+\Delta t}-\varepsilon_{ii}^{init}}{\Delta\varepsilon_{ii}}\right), & \varepsilon_{ii}^{init}\leq\varepsilon_{ii}^{t+\Delta t}<\varepsilon_{ii}^{init}+\Delta\varepsilon_{ii}\\ E_{ii}^{0}\cdot(1-d_i)\dfrac{\varepsilon_{ii}^{init}+\Delta\varepsilon_{ii}}{\varepsilon_{ii}^{t+\Delta t}}, & \varepsilon_{ii}^{t+\Delta t}\geq\varepsilon_{ii}^{init}+\Delta\varepsilon_{ii}\end{cases} \tag{12}$$

where E_{ii}^{0} is the initial modulus of elasticity from Table 1 for lamina orthotropic directions, $\Delta\varepsilon_{ii}$ is a user-defined strain step to ensure a smooth reduction of the properties upon failure and d_i is the reduction factor. Initial failure strain and corresponding stress ε_{ii}^{init}, σ_{ii}^{init} are determined by simulation for FI=1 according to relation (9).

The reduction parameters for E_{ii} (i =1...3) obtained after several parameter tuning and FEA iterations are presented in Table 3.

Table 3. Degradation parameters for longitudinal moduli

Failure mode	d_i	$\Delta\varepsilon_{ii}$
Fiber shear-compression (i = 1)	0.45	0.01
Matrix compression (i = 2,3)	0.57	0.01

- Continuous degradation rules for shear moduli

In post failure analysis, the in-plane shear moduli G_{ij} are reduced using the maximum shear strains $\gamma_{ij}^{t+\Delta t}$ for FI > 1, according to Hashin, [43]:

$$G_{ij}=G_{ij}^{0}\left(0.1+0.9\cdot\frac{\gamma_{ij}^{init}}{\gamma_{ij}^{t+\Delta t}}\right),\ i\neq j=1..3 \tag{13}$$

- Poisson's coefficient reduction

The reduction of the Poisson's ratios is proposed in order to comply with the elastic stability of the orthotropic materials, as suggested in Kolks and Tserpes, [44]:

$$\nu_{12}=\nu_{12}^{0}\cdot\sqrt{\frac{E_{11}E_{22}^{0}}{E_{22}E_{11}^{0}}}\ ,\quad \nu_{13}=\nu_{13}^{0}\cdot\sqrt{\frac{E_{11}E_{33}^{0}}{E_{33}E_{11}^{0}}}\ ,\quad \nu_{23}=\nu_{23}^{0}\cdot\sqrt{\frac{E_{22}E_{33}^{0}}{E_{33}E_{22}^{0}}} \tag{14}$$

These conditions are imposed as to normal stiffness ratios may vary significantly with degradation and the material's stress-strain matrix has to be maintained positive definite and thus allow the FE solver to perform calculations. Assuming constant product of the major Poisson's ratios before and after reduction (degradation) as $\nu_{ij}\cdot\nu_{ji}=\nu_{ij}^{0}\cdot\nu_{ji}^{0}$ and that $\nu_{ij}/\nu_{ji}=E_{ii}/E_{jj}$ relations (14) result.

- SHM method description

A common and useful method for structure health monitoring (SHM) is using the guided waves. The pioneer of this method is Horace Lamb who first published his result in 1917, [45]. There are two types of propagation modes for these waves: symmetric mode (S_0, S_1…S_n) and anti-symmetric (A_0, A_1…A_n), [46]. In usual applications, the most used mode for SHM testing method is the fundamental mode S_0, which has maximum amplitude at high frequency 150-300 Hz and A_0 which has maximum amplitude at low frequency, 30-100 Hz, [47]. The reason for choosing these two fundamental modes is that they are easier to identify from the oscillation group of modes than the higher ones. The SHM testing technique was used to experimentally observe the first ply failure in the laminate plate of the bolted joint. The PWAS devices have a circular shape with 5 mm diameter and are presented in Figure 6. The input signal is a sinusoidal tone burst type signal having 20 V peak to peak amplitude with Hanning window amplitude modulation. This signal includes 3 periods and is generated by an Agilent 33120 signal generator.

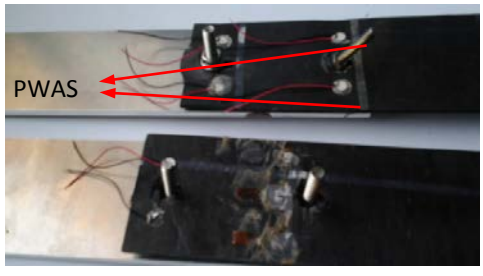

Figure 6. PWAS positions on composite plate

4. RESULTS AND DISCUSSIONS

Figure 7 presents the damage initiation effect on the amplitude of the received signal and force-displacement characteristic curve to identify the first ply failure of the laminated plate of the joint. The amplitude curves represent the maximum (peak to peak) amplitudes of each receiving signals during the test. The input and output signals of the two PWAS's from the laminated plate are obtained with a period of 2 seconds. Figure 7 shows that the amplitude of output signal is increasing with the joint stiffening up to the first lamina failure event. Afterwards the amplitude is decreasing due to the elastic properties degradation in the laminate in the post failure stage. As a conclusion, it can be considered that SHM method accurately predict the first lamina failure and joint limit load which represents the fiber compression damage at the lamina level.

Load-displacement curves for each temperature value are presented in Figures 8 and 9. It can be seen that the temperature has increased the limit (damage initiation) and ultimate (maximum) loads significantly. At point A on the characteristic load-displacement curves, the fiber and matrix compression damages onset around the hole is evident according to Figure. 10. At the beginning of the test, the structural response of the joint is dominated by friction between the plates up to 0.5mm displacement, for T = +50ºC and 0.05mm displacement, for T = - 50ºC. From the end of the friction stage up to point A, the structural behavior of the hybrid joint is almost linear with small fluctuations which represents small matrix compression damages, but this does not affect the overall joint stiffness.

Point A represents the first damage initiation point, denoting the limit load of the joint and is located at the major deviation of the force-displacements curves from linear behavior. At this point, the compression fibers damage is onset as an indicator of the bearing failure initiation. Matrix compression damage is also present at point A, but this does not contribute a lot to the joint stiffness lose, because fibers have the most important role in joint stiffening. As can be seen from Figures 10 and 11, in 0º plies the amount of fibers damage is less than matrix damage, while in 90º plies the two micro level damages have almost the same amount. In (Figures 10-15), the dark blue color represents the undamaged elements, while the red color states for E^0_{ii} (1-d_i) residual stiffness of the elements.

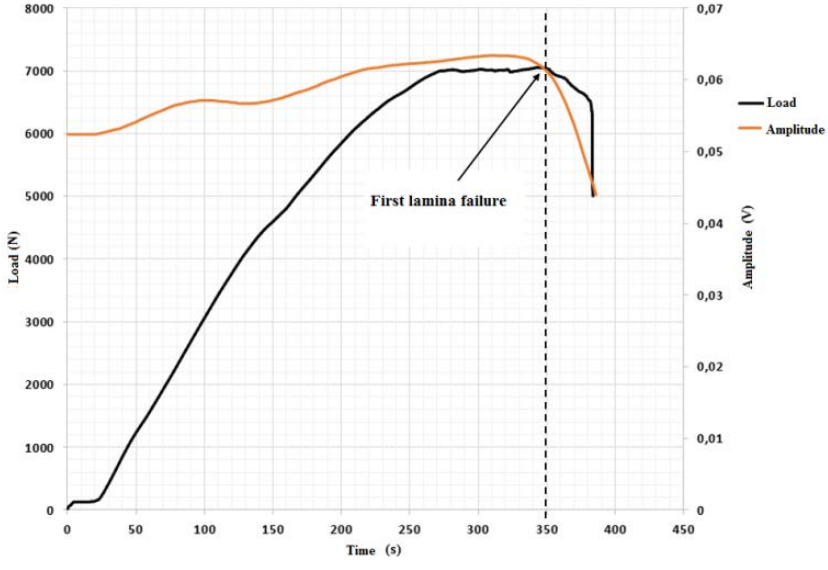

Figure 7. Damage effects on output signal, T = + 50ºC

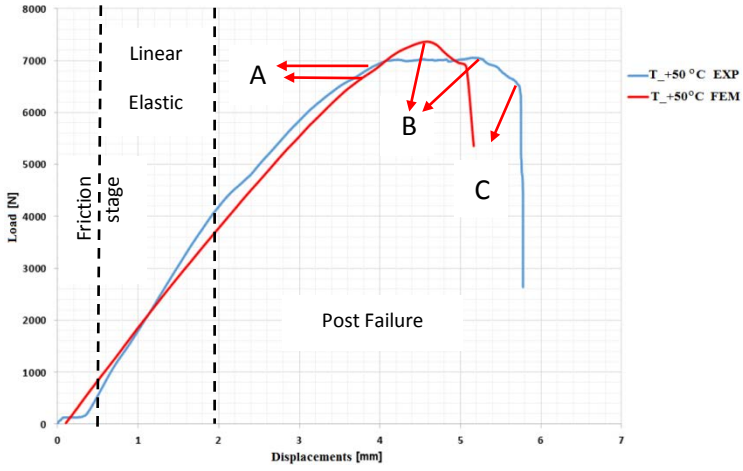

Figure 8. Load-displacement curves, T = + 50ºC

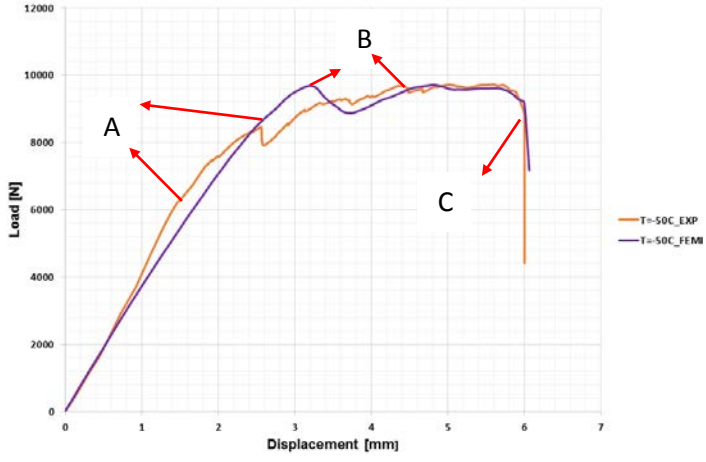

Figure 9. Load-displacement curves, T = - 50ºC

From Figure 14, it can be observed that the friction static force between the aluminum and composite plates is about F_f = 150N and taking into account the plates clamping force P = 330N, implies that the real friction coefficient should be equal to:

$$\mu = \frac{F_f}{2 \cdot P} = \frac{150}{2 \cdot 330} = 0.227 \tag{15}$$

This value is quite closer to the values used in numerical simulations, μ=0.235, according to Schon, [48], which implies that the simulation took into account the friction base phenomena with sufficient accuracy. In Figures 8 and 9 above, point B represents the joint ultimate failure. After the point A, the damage accumulation determines joint stiffness reduction gradually and the characteristic curve becomes nonlinear. From point A up to point B, the post failure stage is completely developed, where the residual stiffness is continuously reduced. On this stage, the fibers and matrix compression and fiber-matrix shear damages are increasing in the bearing plane through the whole thickness of the laminate plate, as can be seen in Figures 11 and 14. Point C represents the catastrophic final failure of the joint, when the above mentioned damages are extended to a large portion of the laminate plate Figures 12 and 15. The thermal effects on the failure modes for the two studied temperatures can be seen in Figure12 and 15, where it is observed that for positive temperature the bearing mode and

shear-out is predominant at protruding head bolt hole, while for negative temperature value, the failure mode is bearing for the both holes.

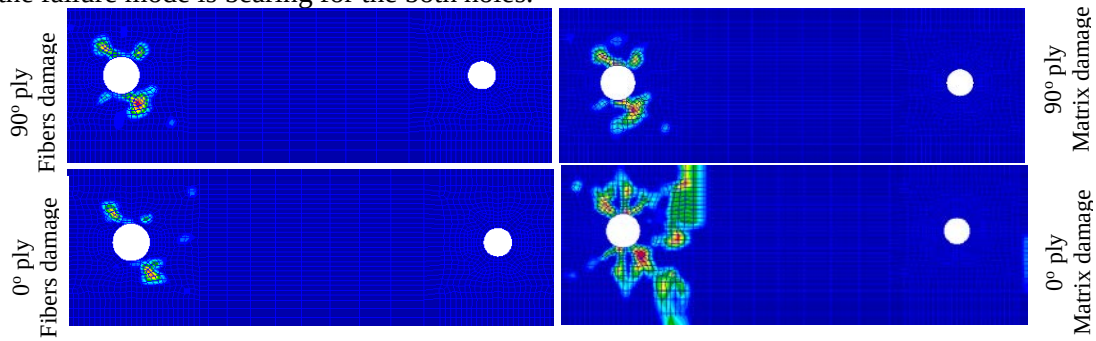

Figure 10. Hole bearing damage onset, point A, T = + 50°C

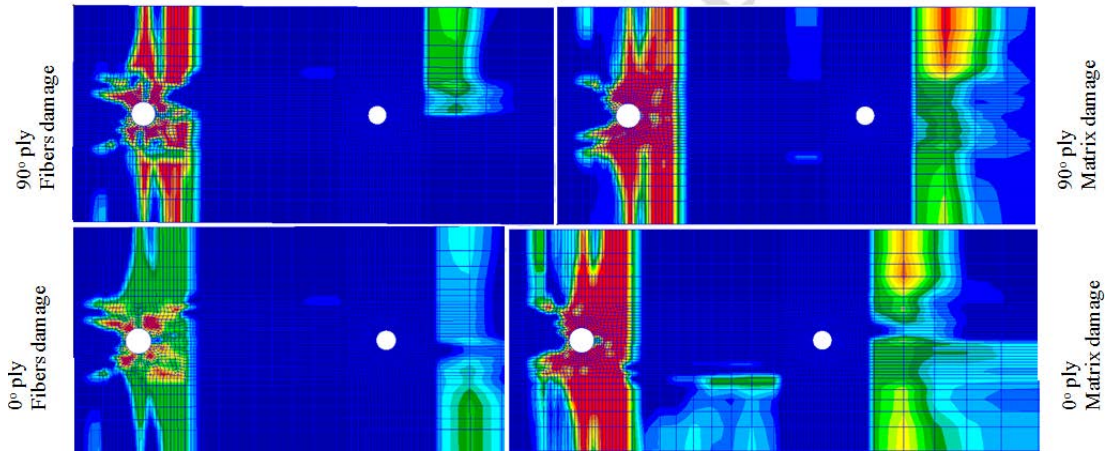

Figure 11. Progressive hole damage, point B, T = + 50°C

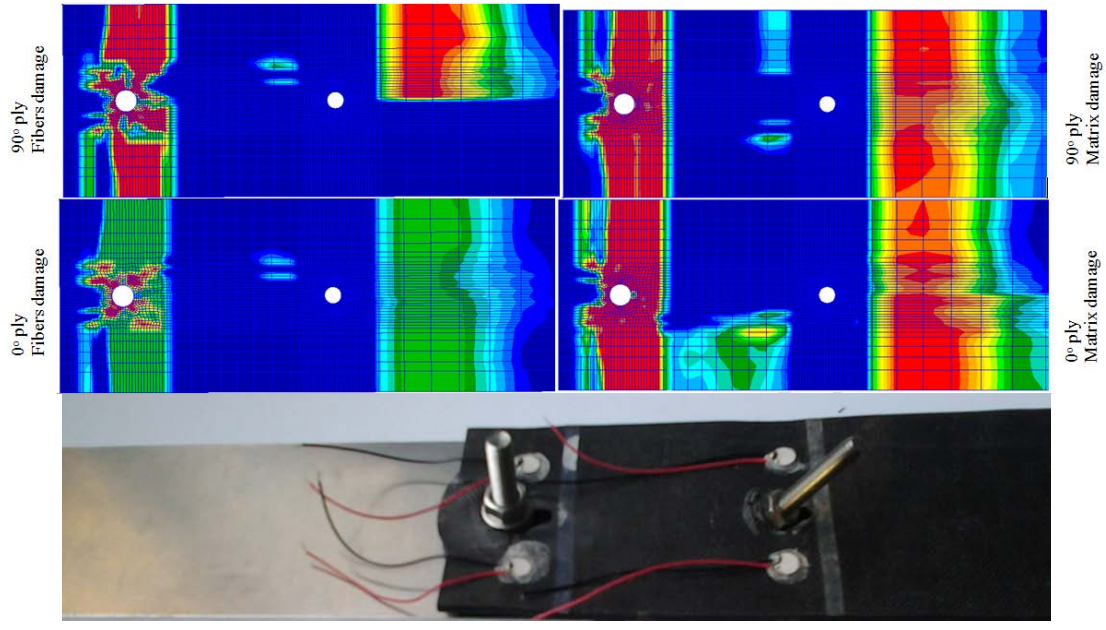

Figure 12. Catastrophic failure, point C, T= + 50°C

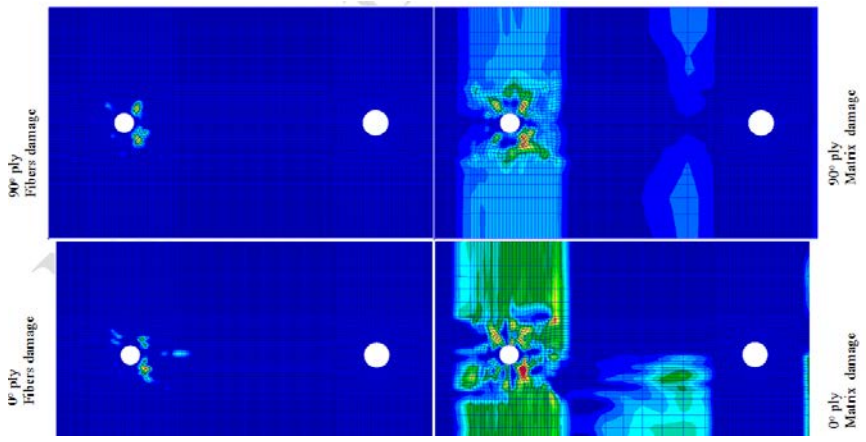

Figure 13. Hole bearing damage, point A, T = - 50°C

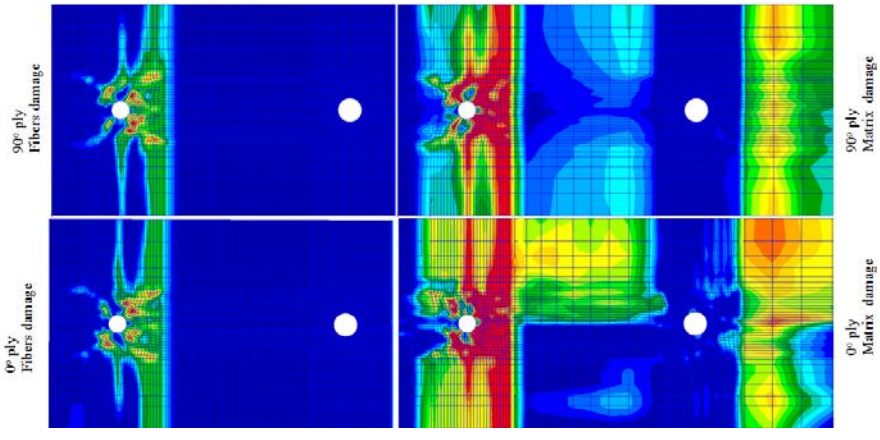

Figure 14. Progressive hole damage, point B, T = - 50°C

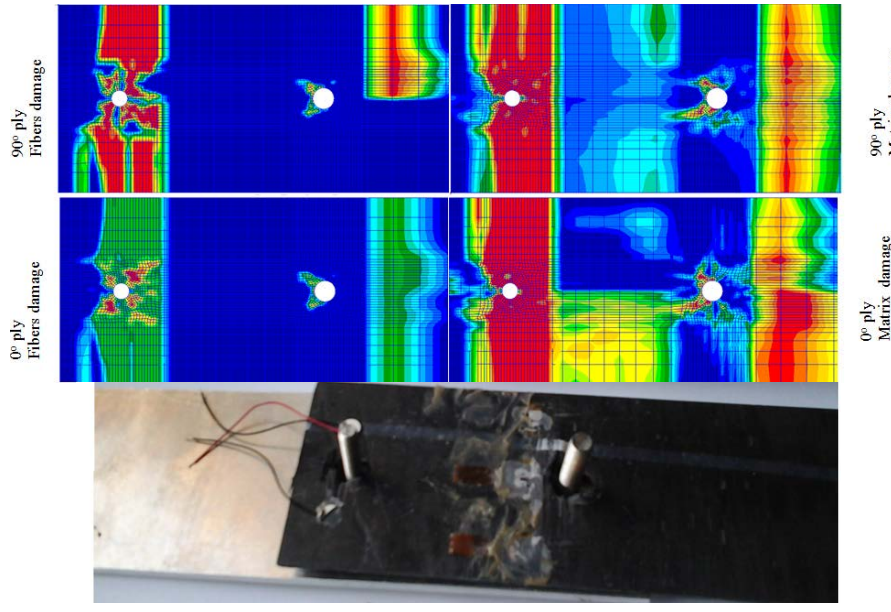

Figure 15. Catastrophic failure, point C, T = - 50°C

A summary of the thermal effects on the failure modes of protruding and countersunk multi-bolts hybrid joints is presented in Table 4 and Figure 16 in terms of limit load (L.L) and ultimate load (U.L.) capacity. From Table 4 it can be seen that the temperature increase reduces the joint strength. The final mode of failure is changing as can be clearly seen in Table 4, for example, for T = - 50^0C the failure mode is bearing while for T = + 50^0C, this is bearing and shear-out mixt mode. In Table 4 it can be observed that negative values of temperature can confer a higher strength of the joint due to the fact that the composite material becomes much stiffen at low temperature.

So, the temperature is a very important parameter in the design process of reliable joints and has to be taken into account very carefully due to the different material thermal expansion coefficients and different modes of failure for positive and negative values of temperature. The joints are designed to fail in ductile bearing mode for the benefits of the stress relief in the hole vicinity. The positive value of temperature has its own benefits, underlying that, for T= + 50°C, it was observed in the experiments the yielding process before the final failure due to the low fiber volume ratio (32 %) in laminate's layers and this yielding contributes to the stress relief.

Table 4 Thermal effects on final failure mode of the joint

Torque [Nm]	Temperature [°C]	F_{LL} [N]		F_{UL} [N]		Failure mode
		EXP	FEM	EXP	FEM	
0.5	+50	6200	6300	7050	7400	Bearing+shear-out
0.5	-50	8400	9800	9830	9815	Bearing

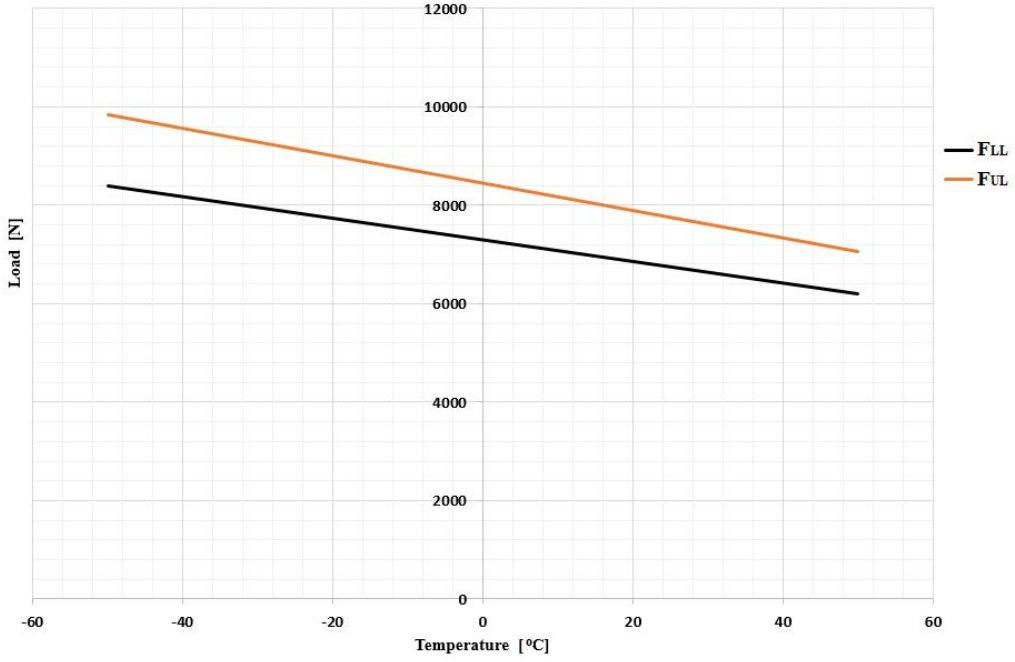

Figure 16. Influence of the temperature on the limit and ultimate load capacity of the joint, experimental results

5. CONCLUSIONS

In this paper, the thermal effects on the stiffness, damage initiation and progressive failure for single-lap, multiple-bolts, hybrid metal-composite joints are investigated using both experimental technique and simulations with finite element method (FEA). Regarding the first

ply failure (FPF) and strength evaluations, a progressive damage analysis (PDA) including lamina nonlinear shear behavior, Hashin's failure criteria and strain-based continuous degradation rules was proposed. A 3D FEM model, which incorporates geometrical and contact full nonlinearities was developed in Patran commercial software as preprocessor and Nastran as explicit iterative solver. The PDA material model was implemented using a user-defined subroutine namely User_mat, using FOTRAN programming language.

The simulation results were in good agreement with the experiments in terms of load-displacement behavior, surface strains, joint stiffness, FPF and ultimate loads, as can be seen in (Figures 12, 13 and 14), which denoted that the 3D FEM model including full nonlinearities and explicit solver are quite accurate and can predict the metal-composite joint's structural behavior on both linear and nonlinear elastic ranges, including the failure modes as bearing and shear-out.

Regarding the thermal effects on the joint stiffness it can be seen from Table 4 that, temperature decreases the stiffness of the joint in the axial direction. The loading joint behavior released some interesting features at the beginning stage due to friction between the plates. This friction stage is composed from two parts: static and dynamic friction as can been seen from the load-displacement curves in Figures 13 and 14. From these graphs it can be detected the friction load and, knowing the clamping force from torque level, therefore the friction coefficient between the plates can be calculated for the two temperatures study. Regarding the influence of temperature on the ultimate load of the joint, it has been observed that the load is decreasing while temperature is increasing, so as a global conclusion of the study, the temperature has reduced both the stiffness and strength of the joint.

ACKNOWLEDGEMENTS

Funding: This work was supported by the EU Structural Funding through "Be Antreprenor!" Project [grant number 51680/09.07.2019POCU/380/6/13-SMIS code: 124539], under the consideration of the "Politehnica" University of Bucharest.

REFERENCES

[1] Y. Xiao, T. Ishikawa, Bearing strength and failure behavior of bolted composite joints (part II: modeling and simulation), *Composites Science and Technology*, vol. **65**, pp. 1032–1043, 2005.

[2] J. L. Chaboche, Continuum damage mechanics: part I – General concepts; part II – damage growth, crack initiation and crack growth, *Journal of Applied Mechanics*, vol. **55**, pp. 59–72, 1988.

[3] F. K. Chang, K. Y. Chang, Post-failure analysis of bolted composite joints in tension or shear-out mode failure, *Journal of Composite Materials*, vol. **21**, pp. 809–833, 1987.

[4] L. B. Lessard, M. M. Shokrieh, Two-dimensional modeling of composite pinned-joint failure, *Journal of Composite Materials*, vol. **29**, pp. 671–697, 1995.

[5] C. L. Hung, F. K. Chang, Bearing failure of bolted composite joints. Part II: model and verification. *Journal of Composite Materials*, vol. **30**, pp. 1359–1400, 1996.

[6] S. J. Kim, J. S. Hwang, J. H. Kim, Progressive failure analysis of pin-loaded laminated composites using penalty finite element method, *AIAA Journal* vol. **36**(1), pp. 75–80, 1998.

[7] P. P. Camanho, F. L. Matthews, A progressive damage model for mechanically fastened joints in composite laminates, *Journal of Composite Materials*, vol. **33**, pp. 2248–2280, 1999.

[8] J. Serra, C. Bouvet, B. Castanie´, et al., Scaling effect in notched composites: the discrete ply model approach, *Composite Structures*, vol. **148**, pp. 127–143, 2016.

[9] L. Adam, C. Bouvet, B. Castanie´, et al., Discrete ply model of circular pull-through test of fasteners in laminates, *Composite Structures*, vol. **94**, pp. 3082–3091, 2012.

[10] P. P. Camanho and M. Lambert, A design methodology for mechanically fastened joints in laminated composite materials, *Composites Science and Technology*, vol. **66**, pp. 3004–3020, 2006.

[11] B. Okutan, The effects of geometric parameters on the failure strength for pin-loaded multi-directional fiberglass reinforced epoxy laminate, *Composites B Engineering*, vol. **33**, pp. 567–578, 2002.
[12] K. I. Tserpes, G. Labeas, P. Papanikos, et al., Strength prediction of bolted joints in graphite/epoxy composite laminates, *Composites B Engineering*, vol. **33**, pp. 521–529, 2002.
[13] A. Olmedo and C. Santiuste, On the prediction of bolted single-lap composite joints, *Composite Structures*, vol. **94**, pp. 2110–2117, 2012.
[14] Z. Kapidz˘ic´, L. Nilsson and H. Ansell, Finite element modeling of mechanically fastened composite-aluminum joints in aircraft structures, *Composite Structures*, vol. **109**, pp. 198–210, 2014.
[15] M. R. Garnich and V. M. K. Akula, Review of degradation models for progressive failure analysis of fiber reinforced polymer composites, *Appl Mech Rev*, vol. **62**, pp. 010801–1–010801-33, 2009.
[16] H. Koerber and P. P. Camanho, *Simulation of progressive damage in bolted composite joints*, In: 13th European conference on composite materials, *ECCM* 13, 2–5 June, Stockholm, Sweden, 2008.
[17] A. K. Zerbst, G. Kuhlmann and C. Steenbock, Progressive damage analysis of composite bolted joints with liquid shim layers using constant and continuous degradation models, *Composite Structures*, vol. **92**, pp. 189–200, 2010.
[18] G. Kolks and K. I. Tserpes, Efficient progressive damage modeling of hybrid composite/titanium bolted joints, *Compos Part A Appl Sci Manuf*, vol. **56**, pp. 51–63, 2014.
[19] A. Du, Y. Liu, H. Zin, et al., Progressive damage analysis of PFRP double-lap bolted joints using explicit finite element method, *Composite Structures*, vol. **152**, pp. 860–869, 2016.
[20] B. Egan, M. A. McCarthy, R. M. Frizzell, et al., Modelling bearing failure in countersunk composite joints under quasi-static loading using 3D explicit finite element analysis, *Composite Structures*, vol. **108**, pp. 963–977, 2014.
[21] A. Olmedo, C. Santiuste and E. Barbero, An analytical model for the secondary bending prediction in singlelap composite bolted-joints, *Composite Structures*, vol. **111**, pp 354–361, 2014.
[22] O. Allix, N. Bahlouli, C. Cluzel, et al., Modelling and identification of temperature dependent mechanical behavior of the elementary ply in carbon/epoxy laminates, *Compos Sci Technol*, vol. **56**, pp. 883–888, 1996.
[23] H. da Costa Mattos, J. Reis, L. Paim, et al., Analysis of a glass fiber reinforced polyurethane composite repair system for corroded pipelines at elevated temperatures, *Composite Structures*, vol. **114**, pp. 117–123, 2014.
[24] J. Reis, J. Coelho, A. Monteiro, et al., Tensile behavior of glass/epoxy laminates at varying strain rates and temperatures. *Composites B Engineering*, vol. **43**, pp. 2041–2046, 2012.
[25] J. Reis, F. Amorim, A. da Silva, et al., Influence of temperature on the behavior of DGEBA (bisphenol A digly cidyl ether) epoxy adhesive, *Int J Adhes Adhes*, vol. **58**, pp. 88–92, 2015.
[26] J. Zhengwen, W. Shui and W. Zhishen, Calculation of energy release rate for adhesive composite/metal joints under mode-I loading considering effect of the non-uniformity, *Composites B Engineering*, vol. **95**, pp. 374–385, 2016.
[27] M. Heshmati, R. Haghani and M. Al-Emrani, Durability of bonded FRP-to-steel joints: effects of moisture, deicing salt solution, temperature and FRP type, *Composites B Engineering*, vol. **119**, pp. 153–167, 2017.
[28] A. Agarwal, S. Foster and E. Hamed, Wet thermomechanical behavior of steel–CFRP joints – an experimental study, *Composites B Engineering*, vol. **83**, pp. 284–296, 2015.
[29] A. Agarwal, S. Foster, E. Hamed, et al., Testing of steel-CFRP adhesive joints under freeze-thaw cycling, In: *Samali B, AttardMand Song C (eds) From Materials to Structures: Advancement through Innovation*. London: Taylor & Francis Group, pp.801–806, 2013.
[30] M. Heshmati, R. Haghani and M. Al-Emrani, Effects of moisture on the long-term performance of adhesively bonded FRP/steel joints used in bridges, *Composites B Engineering*, vol. **92**, pp. 1–16, 2016.
[31] * * * ASTM D 5961, Standard test method for bearing response of polymer matrix composite laminates. *American Society for Testing and Materials*, 2007.
[32] M. Chishti, H. Wang, S. Thomson, et al., Experimental investigation of damage progression and strength of countersunk composite joints, *Composite Structures*, vol. **94**, pp. 865–873, 2012.
[33] * * * ISO 286-2, *Tables of standard tolerance classes and limit deviations for holes and shafts*, Geneva, Switzerland, International Organization for Standardization, 2010.
[34] * * * Toray Carbon Fibers America Inc. Torayca T300, Technical data sheet, *Report no. CFA-001*, USA, 2010.
[35] * * * Ashland Inc. Derakane Momentum 411-350 epoxy venyl ester resin, *Technical Data Sheet* No. 1701 V3F2, USA, 2010.
[36] * * * Federal Aviation Administration, *Metallic materials properties development and standardization*, USA: Federal Aviation Administration, 2010.
[37] * * * ASTM D 3039, *Standard Test Method for Tensile Properties of Polymer Matrix Composite Materials*, ASTM International, 2007.

[38] * * * ASTM D 5379, *Standard Test Method for Shear Propeties of Composite Materials by the V-Notched Beam Method*, ASTM International, 2007.
[39] C.-D. Coman, D. M. Constantinescu, Temperature effects on joint strength and failure modes of hybrid aluminum-composite countersunk bolted joints, *Proceedings of the Institution of Mechanical Engineers, Part L: Journal of Materials: Design and Applications*, vol. **233**, pp. 2204-2218, 2019.
[40] M. A. McCarthy, C. T. McCarthy, L. V. Pawlor, W. F. Stanley, Three-dimensional finite element analysis of single-bolt, single-lap composite bolted joints: part I - model development and validation, *Composite Structure*, vol. **71**, pp. 140–158, 2005.
[41] H. Hahn and S. Tsai, Nonlinear elastic behavior of unidirectional composite laminates, *Journal of Composite Materials*, vol. **7**, pp. 102–118, 1973.
[42] * * * *Structural materials handbook: Design calculation methods and general design aspects*, ECSS-E-HB-32-20, Part 2A 20, 2011.
[43] Z. Hashin, Failure criteria for unidirectional fiber composites, *Journal of Applied Mechanics*, vol. **47**, pp. 329–34, 1980.
[44] Y. Zhou, H. Yazdani-Nezhad, M. A. McCarthy, et al., A study of intra-laminar damage in double-lap, multi-bolt, composite joints with variable clearance using continuum damage mechanics. *Compos Struct*, vol. **116**, pp. 441–452, 2014.
[45] H. Lamb, On Waves in an Elastic Plate, *Proceedings of the Royal Society, Mathematical, Physical and Engineering Sciences*, vol. **93**, pp. 114 – 128, 1917.
[46] V. Giurgiutiu, J. Bao, Embedded Ultrasonic Structural Radar with Piezoelectric Wafer Active Sensors for the NDE of Thin-Wall Structures, *Proceedings of ASME International Mechanical Engineering Congress*, 2002.
[47] V. Giurgiutiu, Lamb wave generation with piezoelectric wafer active sensors for structural health monitoring, *SPIE*, 2003.
[48] J. Schön, Coefficient of friction for aluminum in contact with a carbon fiber epoxy composite, *Tribol Int.*, vol. **37**(5), pp. 395–404, 2004.